Deep learning enables accurate soft tissue deformation estimation *in vivo*

By

Reece Douglass Huff

BS (Boston University) 2021

A report submitted in partial satisfaction of the

requirements for the degree of

Master of Science, Plan II

in

Mechanical Engineering

at the

University of California, Berkeley

Committee in charge:

_____

Professor Grace D. O'Connell, Chair

_____

Professor Carisa Harris-Adamson

Spring 2023

Committee: Reece Douglass Huff
Grace D. O'Connell &
Carisa Harris-Adamson

Deep learning enables accurate soft tissue deformation estimation *in vivo*

Abstract

Image-based deformation measurement, a crucial tool in various engineering challenges including crack propagation, fracture, and fatigue, has also found significant application in biology. Specifically, it has been utilized to monitor tissue deformation within the human body, a critical factor in evaluating its condition during both health and disease. However, accurately measuring tissue deformation *in vivo* is difficult. In this thesis, a novel deep-learning approach for measuring deformation from a sequence images is presented, StrainNet, designed to overcome the limitations of traditional image-based strain analysis techniques in challenging, *in vivo* settings. Utilizing a training set based on real-world clinical observations and image artifacts, StrainNet outperforms traditional techniques on both synthetic test cases with known deformations and real, experimentally collected ultrasound images of flexor tendons undergoing contraction *in vivo*. Findings reveal strong correlations between tendon deformation and applied forces *in vivo*, highlighting the potential for StrainNet to be a valuable tool in the assessment of rehabilitation or disease progression. Additionally, by using real-world data to train our model, StrainNet was able to generalize and reveal correlations with tendon material properties and effort level, providing a more complete understanding of the mechanics of tendons under various physiological loads. Overall, StrainNet demonstrates the effectiveness of using deep learning for image-based strain analysis *in vivo*.

i

Εν οίδα, ότι ουδέν οίδα.

ΣΩΚΡΆΤΗΣ

Contents

List of Figures

List of Tables

Acknowledgments

I am deeply grateful to my advisor, Dr. Grace O'Connell, whose unwavering support, astute guidance, and invaluable mentorship have been integral to my research journey. Dr. O'Connell, your expertise and passion have consistently inspired and motivated me, and I feel truly privileged to have worked under your supervision. I would also like to express my heartfelt appreciation to the esteemed professors involved in this project: Dr. Carisa Harris-Adamson, Dr. Craig Goergen, and Dr. Denny Yu. Your collective contributions and encouragement have been pivotal in shaping my academic path.

A special shoutout goes to Freddie Houghton, whose camaraderie, positive attitude, and unwavering commitment truly helped shape and grow this project. Freddie, your tireless efforts in debugging stripy strain maps have been indispensable to the realization of this thesis. I also want to acknowledge Fredy Loaiza, who generously shared his knowledge and expertise in coding, image analysis, texture correlation, Git, and more, providing me with the fundamental skills essential to this thesis. The Freddie/Fredy duo has played a significant role in my research journey.

I would like to extend my gratitude to Dr. Elise Morgan, whose brilliance and propensity for asking challenging questions have shaped my approach to research. Additionally, I want to thank Dr. Paul Barbone, the mathematical wizard whose expertise in mechanics has been the foundation of my work; I still number my equations in every assignment!

I am grateful for the dedication and enthusiasm of the undergraduate student I advised, Ishan Dogra. Your valuable contributions to this project and eagerness to learn have been inspiring.

Last but certainly not least, I am grateful to my labmates across institutions: at Berkeley, including Jonathan McKinley, Erin Archibeck, Melissa Abed, Minhao Zhou, Shiyin Lim, Emily Lindberg, Andre Montes, Yishu Yan, Amber Young, Ben Werbner, Gabriel Lopez, and Tongge Wu; at Boston University, with Neil Frings, Josh Auger, Andre Gutierrez Marty, Yuanqiao Wu, Aldair Gongora, Tim Josephson, Amartya Naik, Ingmar Fleps, Jack Kendall, and Rohin Banerji; and at Purdue, alongside Conner Earl, Elnaz Ghajar-Rahimi, Andrew Darling, Frederick Damen, and Gouyang Zhou. Your collaboration, friendship, and generosity in sharing your knowledge have greatly enriched my experience and made this thesis a reality. I am truly thankful for the support system we have built together and am honored to have been part of such an exceptional team.

1
Introduction

Measuring how things deform is challenging. Image-based deformation measurement has been employed in a multitude of engineering problems, such as crack propagation[28], fracture[21], and fatigue[30]. In the medical field, these techniques have contributed to cancer diagnosis[15,16], injury mechanism assessment[19], and cardiovascular pathology evaluation[12,18]. The demand for non-

invasive *in vivo* deformation tracking has grown due to its potential for assessing rehabilitation or disease progression. However, accurate strain measurement with medical images *in vivo* is challenging due to limited image resolution and the presence of artifacts that can affect accuracy[43]. Consequently, techniques that excel under *in vivo* conditions have become increasingly important.

Overview

This thesis introduces a novel deep-learning approach, `StrainNet`, designed to maximize performance of image-based deformation estimation in challenging, *in vivo* settings. To begin, a comprehensive background of the biological tissue of investigation, flexor tendons, and image texture correlation techniques is provided before delving into the details of `StrainNet`. Robust evaluation and experimental results of our tests and validations, demonstrating `StrainNet`'s potential in predicting strains accurately in both synthetic and real datasets of ultrasound images of tendons *in vivo*.

Contributions

This thesis greatly benefited from the significant contributions of several researchers.

Frederick Houghton, in particular, was instrumental in conducting all image analysis. His work involved the utilization of traditional image correlation algorithms—digital image correlation (DIC) and direct deformation estimation (DDE). These methods are elaborated in **Section 2.2.1** and **Section 2.2.2** respectively. Frederick's application of DIC and DDE spanned across all synthetic test

cases presented in **Appendix D**, as well as the analysis of images gathered experimentally, as outlined in **Section 3.4**. Beyond this, Frederick's expertise was crucial in both the conception of the experimental protocol and the design of a custom jig, detailed in **Section 3.2**.

In the realm of data collection, **Conner Earl, Elnaz Ghajar-Rahimi, and Gouyang Zhou** provided indispensable assistance. They were responsible for acquiring all experimental images and undertaking force measurements. Their methods and contributions are further discussed in **Section 3.2** and **Appendix C.2**.

2
Background

THIS CHAPTER COVERS ESSENTIAL BACKGROUND INFORMATION in tendon mechanics and image texture correlation techniques while setting the stage for the introduction of `StrainNet`.

2.1 Tendon mechanics

Tendons play a crucial role in the musculoskeletal system, transmitting force from muscles to bones to facilitate movement. Understanding tendon mechanics is vital for diagnosing and treating various tendon-related pathologies and injuries, as well as for designing improved prosthetic devices. Both *in vivo* and *in vitro* studies can provide valuable insights into tendon properties and behavior under different loading conditions. In this section, existing literature on *in vivo* studies of tendon mechanical behavior was reviewed, highlighting key findings, the experimental design, and the techniques utilized.

When investigating tendon mechanics, many researchers have focused on examining maximum tendon strain under various loading conditions. For instance, Sheehan et al.[40] reported that the average maximum strain in the human patellar tendon was 6.6%, with strains reaching up to 11%. Their study involved flexing the knee to 40° flexion at 35 cycles per minute while resisting a 34N weight, and they used a piece-wise strain calculation to ensure that the strain measurements were tensile. Gerus et al.[14] applied an image texture correlation algorithm to ultrasound images of medial gastrocnemius tendon under tension and found that strains ranged from 8-11%. O'Brien et al.[31] discovered that *in vivo* strain in human patellar tendons ranged from 4% to 14%, depending on the loading and gender. Additionally, Lee et al.[23] demonstrated that human patellar tendon strain was dependent on the depth of the strain measurement, with strains deep within the tendon being significantly higher than those on the surface. These studies underscore the complexity and variability

of tendon strain under different conditions, highlighting the importance of accounting for factors such as measurement depth when investigating tendon mechanics.

In addition to strain, the tendon apparent modulus has been a key area of interest of researchers. Table 2.1 provides a comparison of the *in vivo* reported apparent moduli of different human tendons under various loading conditions. The patellar tendon, as investigated by Carroll et al.[7], Reeves et al.[36], and Hansen et al.[17], exhibited apparent moduli of 0.9 GPa, 1.3 GPa, and 1.09 GPa, respectively, under conditions of maximal isometric knee extension, with slight variations in the testing approach. The Achilles tendon, studied by Lichtwark & Wilson[24] and Coombes et al.[8], showed a slightly lower apparent modulus with values of 0.87 GPa and 0.76 GPa, respectively, under the conditions of one leg hopping and maximum voluntary isometric plantarflexion contractions. The tibialis anterior tendon, tested by Maganaris & Paul[27] using 50V applied and maximum isometric load, showed the most varied modulus, with values of 0.45 GPa and 1.2 GPa. Finally, the tendon structures in the vastus lateralis muscle, as investigated by Kubo et al.[22], presented the lowest apparent modulus values of 0.29 GPa and 0.43 GPa under the condition of isometric knee extension torque from a relaxed state to maximum voluntary contraction within 5 seconds.

These studies offer valuable insights into the mechanical behavior of tendons *in vivo*. The results indicate that tendons can experience considerable maximum strains, ranging from 6.6% to 14%[14,23,31,40]. This highlights the importance of considering the depth of strain measurement, as strains deep within tendons can be significantly higher than those on the surface. Simultaneously, the apparent modulus provides insights into the inherent stiffness of the tendon tissue, demonstrating variability across different tendons and under diverse loading conditions. The apparent modulus

of these tendons, as shown in Table 2.1, also exhibits considerable variation[7,8,17,22,24,27,36].

Table 2.1: Comparison of *in vivo* reported mechanical properties of different human tendons under different loading conditions.

author	tendon	loading condition	apparent modulus (GPa)
Carroll et al.	patellar	maximal 10-s ramp isometric knee extension	0.9 ± 0.1
Reeves et al.	patellar	maximal isometric knee extension	1.3 ± 0.3
Hansen et al.	patellar	maximal 10-s ramp isometric knee extension	1.09 ± 0.12
Lichtwark & Wilson	achilles	one leg hopping	0.87 ± 0.2
Coombes et al.	achilles	maximum voluntary isometric plantarflexion contractions	0.76 ± 0.4
Maganaris & Paul	tibialis anterior	50V applied & maximum isometric load	0.45 ± 0.06 & 1.2 ± 0.15
Kubo et al.	tendon structures in the vastus lateralis muscle	isometric knee extension torque from zero (relax) to MVC within 5 s	0.29 ± 0.03 & 0.43 ± 0.04

2.2 IMAGE TEXTURE CORRELATION

IMAGE TEXTURE CORRELATION—or optical flow—is a prevalent image processing technique, originating in the 1980s[20,26,35]. This method fundamentally hinges on determining the displacement field between pixels of a reference (or "undeformed") image and a "deformed" image (**Figure 2.1a**). This is achieved by employing a cost function, which can take the form of either a correlation or a loss function. The technique presupposes that pixel values, such as intensity, remain constant between the undeformed and deformed images. Two prominent variants of image texture correlation are described below.

2.2.1 DIGITAL IMAGE CORRELATION (DIC)

Digital image correlation (DIC) is an extensively utilized image texture correlation method. It operates by dividing the reference images into a grid of rectangular boxes. The size of the box is often denoted as the subset size, while the spacing between the subsets is commonly referred to as the step size (**Figure 2.1b**). DIC employs the cost function

$$\mathcal{C}_{\mathrm{DIC}}[\mathbf{U}_i] = \int_{\Omega_i} \left[\mathrm{I}_1(\mathbf{X}_i) - \mathrm{I}_2(\mathbf{X}_i + \mathbf{U}_i) \right]^2$$

where I_1 and I_2 are the reference and deformed images, respectively, and $\mathbf{X}_i$ and $\mathbf{u}_i$ represents the pixel coordinates and displacement centered in subset Ω_i. Cost functions can be applied either

locally (independently for each subset) or globally (enforcing displacement continuity among neighboring subsets). The discrete displacement field is then numerically differentiated to obtain a discrete strain field (**Figure 2.1b**). Palanca et al. provides a comprehensive review of DIC applications in biomechanical engineering.

2.2.2 DIRECT DEFORMATION ESTIMATION (DDE)

Direct deformation estimation (DDE) is similar to DIC in many aspects, but with a crucial difference: instead of calculating the displacement field, DDE determines the deformation gradient, $\mathbf{F}$, which maps the undeformed and deformed images via $d\mathbf{x} = \mathbf{F}d\mathbf{X}$ (**Figure 2.1c**). The cost function utilized in DDE is of the form

$$\mathcal{C}_{\mathrm{DDE}}[\mathbf{U}_i] = \int_{\Omega_i} \left[\mathrm{I}_1(d\mathbf{X}_i) - \mathrm{I}_2(d\mathbf{x}_i + \mathbf{F}_i d\mathbf{X}_i)) \right]^2$$

where $d\mathbf{X}_i$ and $d\mathbf{x}_i$ denotes the change in pixel coordinates in the reference and deformed image, respectively, and $\mathbf{F}_i$ represents the deformation gradient in subset Ω_i. By directly computing the strain from the deformation gradient without the need for displacement differentiation, DDE has been shown to provide better accuracy, noise insensitivity, and precision compared to displacement-based techniques like DIC[6].

9

2.2.3 Limitations of image texture correlation

Despite the widespread use and success of image texture correlation techniques, such as digital image correlation (DIC)[43] and direct deformation estimation (DDE)[5,6], they are not without their limitations. Some of the main drawbacks of these techniques include noise sensitivity, the need for sufficient texture, and the inability to handle large deformations. These limitations are discussed in detail below.

Noise Sensitivity: One of the significant limitations of image texture correlation techniques is their sensitivity to image noise[13]. The fundamental assumption behind these methods is that the image intensity, remain constant between the undeformed and deformed images[39]. However, in real-world scenarios, images are often affected by various types of noise, such as sensor noise or environmental noise[3]. This noise can lead to errors in the estimation of displacement and strain fields, ultimately affecting the accuracy of the results[49,50]. Several strategies have been proposed to mitigate the effect of noise, such as the use of pre-processing techniques to denoise images[29], incorporating regularization terms in the cost function[21], and employing robust optimization algorithms[33].

Texture requirement: Adequate image texture is a prerequisite for accurate displacement and deformation measurements using image texture correlation[46]. When images present low or uniform texture, the accuracy of these techniques can be compromised. To mitigate this, researchers have proposed the use of artificial speckle patterns or markers to increase image texture[42]. Also, the adoption of advanced image processing algorithms, capable of extracting subtle texture details, has been recommended[2]. Ensuring the overall accuracy of image correlation techniques under varied textures

is pivotal for enhancing their applicability and precision across various fields [2,42,46].

Large deformation handling: Traditional image texture correlation techniques often struggle to handle large deformations or complex motion between the undeformed and deformed images. This limitation arises due to the linear approximation employed in the cost functions, which may not accurately capture the non-linear deformations present in the images [11]. To overcome this issue, researchers have developed multi-scale and multi-resolution approaches, where the deformation estimation is performed iteratively at various scales and resolutions, starting from a coarse scale and gradually refining the estimate at finer scales [25].

In conclusion, while image texture correlation techniques have proven to be valuable tools for deformation and displacement estimation, they have several limitations. Researchers have been continuously working to address these challenges and develop more advanced and robust techniques for a wide range of applications.

2.3 ADVANCES IN MACHINE LEARNING

IN RECENT YEARS, the development of advanced algorithms and computational methods has greatly improved the performance of image-based deformation measurement techniques [9,45]. Deep learning techniques have been introduced to enhance the pattern matching process, enabling more accurate and robust displacement estimations even in the presence of noise and other distortions [41]. Additionally, real-time processing capabilities are being developed to facilitate faster, more efficient

measurements[1].

Recent developments in machine learning have shown promise in measuring strains from images over traditional strain measurement methods. In particular, deep learning techniques, such as convolutional neural networks (CNNs), have been applied to predict strain maps between successive images[4,48,51]. These methods have been shown to provide more accurate and robust results compared to traditional image texture correlation techniques, such as DIC, in controlled settings[51]. One of the key advantages of using deep learning for image-based strain measurement is that the model can be trained on a large dataset of image pairs with known strains, allowing the model to "learn" to overcome image artifacts that can negatively impact the accuracy of traditional techniques[51].

2.4 StrainNet

CONSIDERING THE LIMITATIONS OF IMAGE TEXTURE CORRELATION and recent advancements in machine learning, we introduce a novel deep-learning approach called StrainNet, specifically designed to maximize performance in challenging, *in vivo* settings. In order to test and validate our approach, we limit ourselves to one biological domain—*in vivo* flexor tendon undergoing contraction.

StrainNet leverages the power of CNNs to accurately predict full-field strain maps from image pairs captured during *in vivo* ultrasound imaging of tendons (**Figure 2.1d**). Its robustness and adaptability allow it to overcome challenges such as low image quality and complex tendon move-

ments, making it a valuable tool for tendon mechanics research. The remainder of this thesis will present the development, implementation, and validation of `StrainNet` in the context of tendon mechanics research, as well as its potential applications in other fields where image-based strain measurement is crucial.
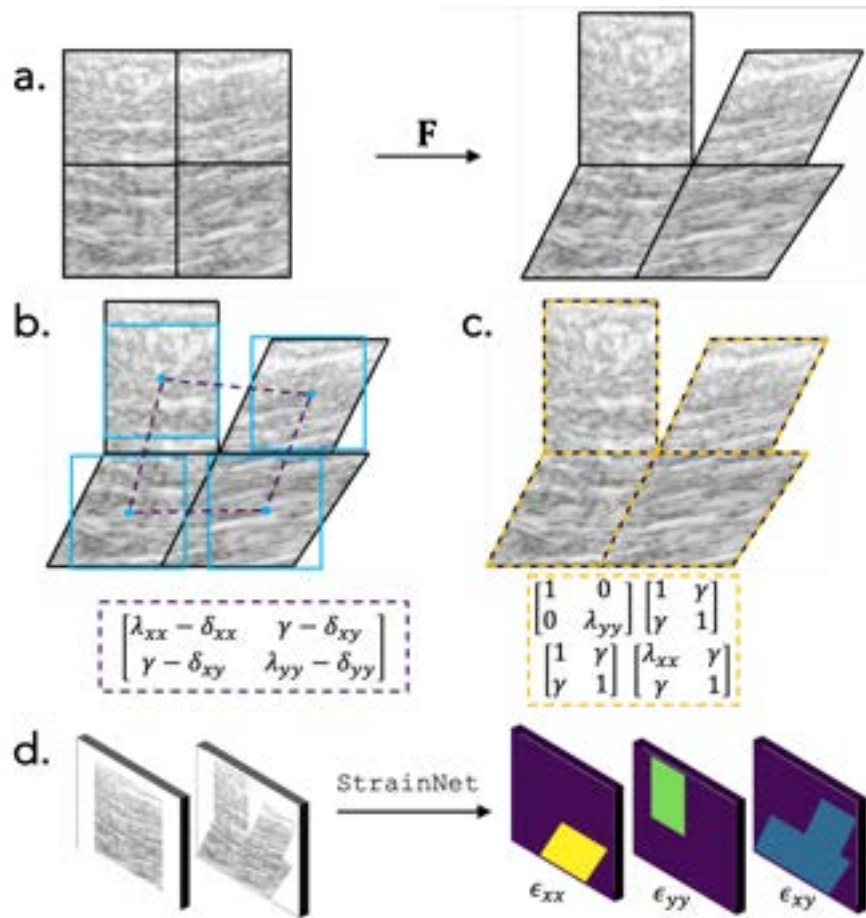
Figure 2.1: Schematic illustrating the process of strain calculation using DIC, DDE, and `StrainNet` from an image pair. **a.** The left image represents a reference image (i.e., I_1), and the right image represents a deformed image (i.e., I_2) exhibiting vertical tension in the top left (λ_{yy}), pure shear in the top right and lower left (γ), and a combination of shear with horizontal extension in the lower right corner (λ_{xx} and γ). **b.** DIC solves for displacements of four pixels using square subset regions (blue boxes) and employs numerical differentiation to estimate strain (dark purple dashed box). $\delta_{\alpha\beta}$ represents the errors from numerical differentiation. **c.** DDE solves for the deformation gradient of each subset directly (orange dashed box). **d.** `StrainNet` estimates full-field strain given a pair of input images (I_1 and I_2).

3

Approach

3.1 StrainNet ARCHITECTURE & TRAINING

THE StrainNet ARCHITECTURE WAS SPECIFICALLY DESIGNED to handle the unique challenges

present with *in vivo* image analysis. Specifically, StrainNet was developed and trained to predict

strain within high-frequency ultrasound images of human *flexor digitorum superficialis* (FDS) ten-
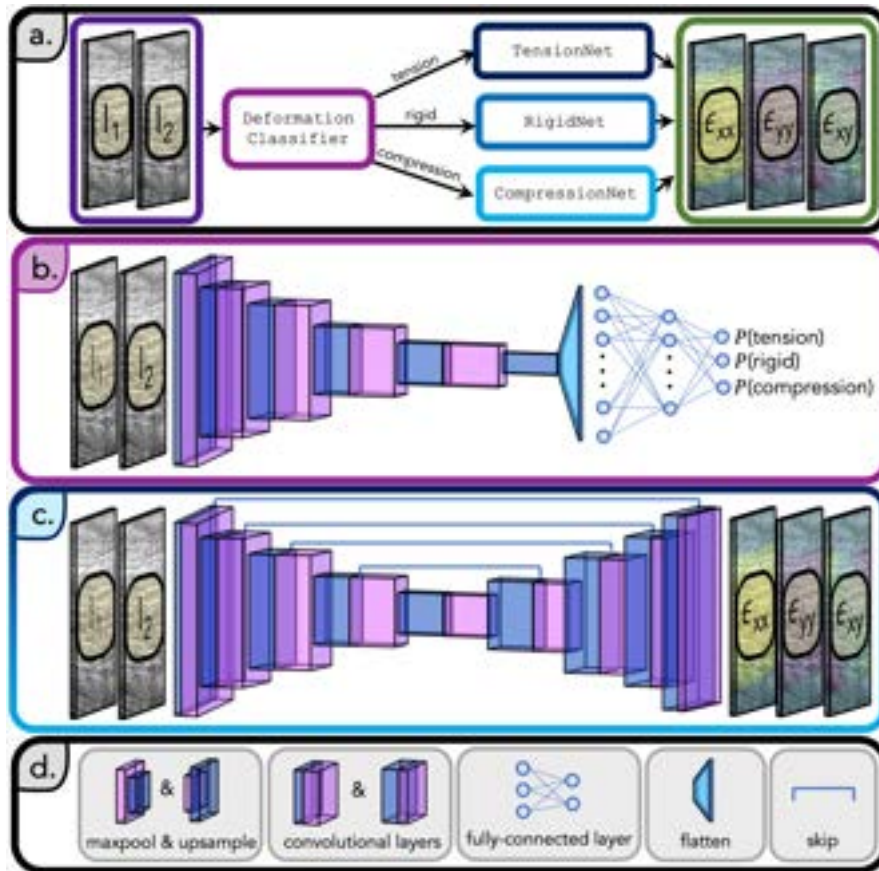
Figure 3.1: Architecture of `StrainNet`. a. `StrainNet` comprises two stages: the first stage is the *Deformation-Classifier*, and the second stage includes `TensionNet`, `CompressionNet`, and `RigidNet`. **b.** The architecture of `DeformationClassifier` is composed of convolutional layers, max pooling, and ReLU activation functions. The resulting features are flattened and passed through a fully-connected neural network to predict the probability of the image pair undergoing tension, compression, or rigid body motions. **c.** The architecture of `TensionNet`, `CompressionNet`, and `RigidNet` includes convolutional layers, max pooling, upsampling, skip layers, and ReLU activation functions, and predicts the full strain field (ε_{xx}, ε_{xy}, ε_{yy}) between the two input images. **d.** Blocks in **b.** and **c.**, all of which are connected by ReLU activation functions and utilize batch normalization.

dons undergoing contraction, as described in a subsequent section (**Section 3.2**) The main idea behind the architecture was to first classify the image pair as undergoing tension, compression, or rigid body motion, and then to apply an appropriate neural network to predict the strain field within the tendon in the ultrasound image (**Figure 3.1a.**).

15

The first stage of the architecture was the `DeformationClassifier`, which was a convolutional neural network (CNN) that classifies the image pair based on the type of deformation (**Figure 3.1a.**). It consisted of a series of convolutional layers, max-pooling layers, and fully connected layers. The convolutional layers extracted features from the image, while the max-pooling layers reduced dimensionality. The fully connected layers were used to make the final classification (**Figure 3.1b.**).

Once the image pair was classified, it was passed to one of three neural networks: `TensionNet`, `CompressionNet`, or `RigidNet` (**Figure 3.1a.**). These networks predict the strain field from the input image pair and were based on the UNet architecture, a popular biomedical image segmentation deep-learning architecture[37]. The UNet architecture has an encoder-decoder structure, with the encoder extracting features and the decoder up-sampling feature maps to the original image size. The encoder and decoder in `TensionNet`, `CompressionNet`, and `RigidNet` were composed of convolutional layers, max-pooling layers, up-sampling layers, and ReLU activation functions (**Figure 3.1c.-d.**). Skip connections between the encoder and decoder were included to help improve strain field prediction quality by reducing vanishing gradients[10].

In order to effectively train `StrainNet`, a diverse training set consisting of 5,000 image pairs that emulate real-world observations and image artifacts commonly encountered in medical imaging was developed. The training set, designed to be representative of the challenging *in vivo* settings, included 3,750 synthetically generated image pairs and 1,250 experimental image pairs. The process of generating the training set involved developing a generalized mathematical model of tendon mechanics based on *in vivo* observations, artificially imposing non-linear strain fields onto collected ultrasound images, and adding noise to simulate real-world imaging conditions (**Appendix B**). These

images were processed and combined to ensure a robust dataset for learning the strain measurement task. The detailed process of generating the training set, including the acquisition of experimental data, image preprocessing, and the combination of synthetic and experimental examples, can be found in **Appendix C**.

Following the creation of the training set, the `StrainNet` model was trained using a combination of loss functions tailored to the specific tasks of each subnetwork. For the `DeformationClassifier`, a cross-entropy loss function was utilized and defined as

$$\mathcal{L}_{\text{CE}}(p, y) = - \sum_{i=1}^{C} y_i \log(p_i), \tag{3.1}$$

where p represents the predicted class probabilities, y is the true one-hot encoded class label, and C is the number of classes (tension, rigid, and compression).

For the other three models, `TensionNet`, `CompressionNet`, and `RigidNet`, the mean ℓ_2 loss function was used and expressed as

$$\mathcal{L}_{\ell_2}(\varepsilon^{pred}, \varepsilon^{true}) = \frac{1}{N} \sum_{i=1}^{N} \sum_{j=1}^{3} \left| \varepsilon_{i,j}^{pred} - \varepsilon_{i,j}^{pred} \right|^2, \tag{3.2}$$

where $\varepsilon_{i,j}^{pred}$ and $\varepsilon_{i,j}^{true}$ denote i-th sample and the j-th component (longitudinal, transverse, and shear across all image pixels) of the predicted and true strain field, respectively, and N is the number of examples in the training batch.

The training process was conducted for 100 epochs using the Adam optimizer (PyTorch [34]

1.12.1) on a K100 16GB NVIDIA GPU with a learning rate of 0.001. Different batch sizes were employed for the sub-models to accommodate their specific training requirements. For the `DeformationClassifier`, a batch size of 100 was used to take advantage of parallel processing and to reduce the noise in gradient updates. In contrast, a smaller batch size of 10 was utilized for the `TensionNet`, `CompressionNet`, and `RigidNet` models, allowing for more frequent weight updates and improved convergence properties. The combination of these hyperparameters, the GPU, and the optimizer facilitated successful training of `StrainNet`, enabling it to learn the relationships between ultrasound images of tendons and their corresponding strain fields.

3.2   HUMAN FLEXOR TENDONS UNDERGOING CONTRACTION
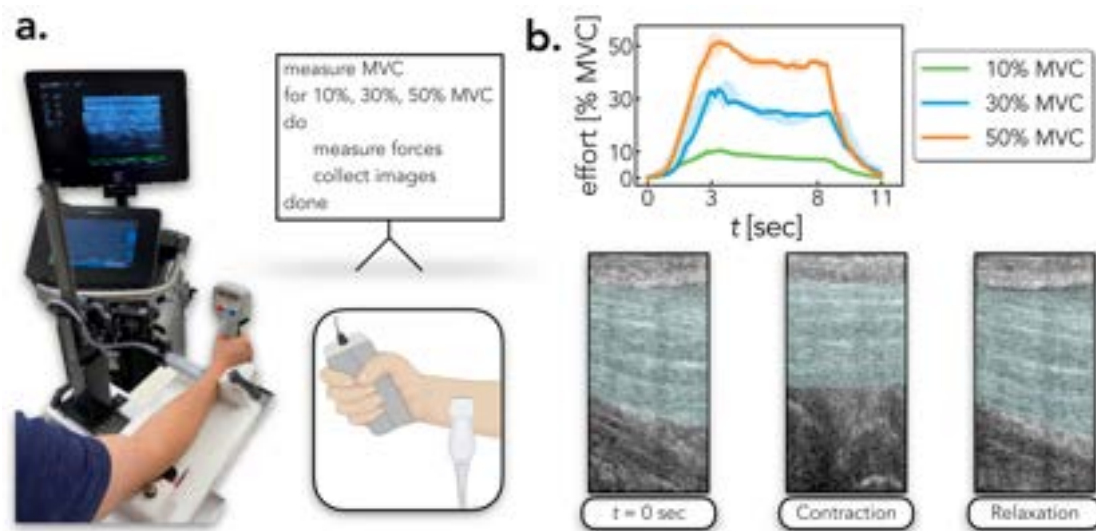
Figure 3.2: Experimental protocol and measured forces and images. a. The custom mount with the participant isometric contractions while the dynamometer measured forces and high-frequency ultrasound images were collected. A zoomed view of the participant's forearm with the dynamometer and the ultrasound probe to facilitate visualization. **b.** Measured effort level over time for 10%, 30%, and 50% MVC, and representative ultrasound images of the flexor tendon throughout the experimental procedure.

18

To evaluate StrainNet's capability of accurately predicting tissue deformation *in vivo*, a participant performed isometric contractions while high-frequency ultrasound images were collected, and a digital dynamometer was utilized to measure the applied forces (Vevo3100 Ultrasound Imaging System, FUJIFILM VisualSonics Inc., Toronto, Ontario, Canada; 21 MHz center frequency linear array ultrasound transducer; 15-30 MHz bandwidth; MX250 and Micro-FET, Hoggan Scientific, Salt Lake City, UT, USA). Throughout the trial, the participant's forearm was secured in a custom-designed apparatus to minimize out-of-plane tendon displacement (**Figure 3.2a.**). The participant's maximum voluntary contraction (MVC) was measured as 289.8N (n = 3 trials). From there, the participant was asked to contract their forearms to their different effort levels—10%, 30%, and 50% of their MVC—in three seconds, hold the contraction for five seconds, and relax in three seconds (**Figure 3.2a.**). Each effort level was repeated five times for a total of fifteen trials (n = 15), all of which were performed with Purdue Institutional Review Board approval (IRB-2020-497). The measured effort levels during testing agreed well with the requested MVC levels; the mean difference between desired and measured MVC was 16% (**Figure 3.2b.**; **Appendix A**). However, two trials were discarded due to corruption of the data file of measured forces (n=13).

3.3   Strain analysis method tuning and validation

In addition to the *in vivo* images, five synthetic test cases were created by artificially imposing a non-linear strain field onto a subset of the collected ultrasound images, in order to quantify

the accuracy of our strain analysis method in a controlled environment where the applied strain was known. These test cases were designed to emulate the process of contraction and relaxation in the experimental procedure described above. Additionally, the prescribed non-linear strain field was designed to reflect reported observations for *in vivo* tendon mechanics (**Section 2.1**). Specifically, the strain in the superficial layer was set to 75% of the deep layer[23], and the tendon was modeled as an incompressible material[44,47]. The five test cases differed in their maximum longitudinal strain, ε_{long}^{max}, which was set to 4%, 7%, 10%, 13%, and 16% to cover the range of strains observed *in vivo*[23,31,40,47]. Additive Gaussian white noise was added to all synthetic test cases to simulate the level of noise present in the experimental dataset. A complete description of the synthetic test cases is provided in **Appendix D**).

The performance and accuracy of `StrainNet` was then benchmarked against to two existing texture correlation algorithms—digital image correlation (DIC)[43] and direct deformation estimation (DDE)[5]—by applying each technique to all of the synthetic test cases. Given the applied strain tensor, the spatial strain error was calculated as

$$\text{spatial strain error} = \sqrt{\sum_{i=1}^{2} \sum_{j=1}^{2} \left(\varepsilon_{ij}^{pred} - \varepsilon_{ij}^{true} \right)^2} \qquad (3.3)$$

where ε_{ij}^{pred} and ε_{ij}^{true} represent the true and predicted strain tensor at a particular pixel within one ultrasound image. To robustly evaluate the performance throughout the test cases, the strain error

and median strain error were calculated as

$$\text{strain error} = \underset{x}{\text{median}} \quad \text{spatial strain error} \qquad (3.4)$$

$$\text{median strain error} = \underset{x,t}{\text{median}} \quad \text{spatial strain error} \qquad (3.5)$$

where the underset x and x, t denote that the median was obtained across the entire ultrasound image or all ultrasound images throughout the full contraction-relaxation cycle, respectively. To compare the strain error for each synthetic test case between `StrainNet` and DIC, as well as between `StrainNet` and DDE, permutation tests of the strain errors were conducted for each test case with a significance level set at 0.05.

3.4 EXPERIMENTAL STRAIN ANALYSIS AND MECHANICAL PROPERTY ESTIMATION

`StrainNet`, DIC, AND DDE WERE THEN APPLIED TO THE EXPERIMENTAL IMAGES. To quantify the bulk tendon mechanical behaviour, the bulk longitudinal strain during the hold period (3-8 seconds) was calculated as the median longitudinal strain over the tendon region:

$$\text{bulk longitudinal strain} = \underset{x_{\text{tendon}},t}{\text{median}} \left. \varepsilon_{long}^{pred} \right|_{3 \text{ sec} \leq t \leq 8 \text{ sec}} \qquad (3.6)$$

Next, linear regression analysis was performed to examine the relationship between the effort level and the corresponding bulk longitudinal strain for each of the three strain analysis methods (`StrainNet`,

DIC, and DDE). The Pearson correlation coefficient (r) and its corresponding p-value were computed to assess the strength and significance of the linear relationship, respectively.

The bulk longitudinal strains were used to estimate the mechanical properties of the tendon. First, the longitudinal tendon stress was calculated by divided the measured force by the tendon's cross-sectional area, which was manually segmented from ultrasound images. Subsequently, the tendon's apparent modulus was calculated as the slope of the linear region of each trial's stress-strain curve. Finally, linear regression on the measured apparent modulus and the effort level was performed with a significance level set at 0.05.

4

Findings

4.1 `StrainNet` OUTPERFORMS TRADITIONAL TECHNIQUES IN CONTROLLED ENVIRON-

MENTS

`StrainNet` significantly outperformed the traditional texture correlation algorithms, DIC and

DDE, in all synthetic test cases; the median strain error from `StrainNet` was 48-84% lower than the

strain error from both DIC and DDE (**Figure 4.1a.**; p<0.001 in all strain cases). In addition to the
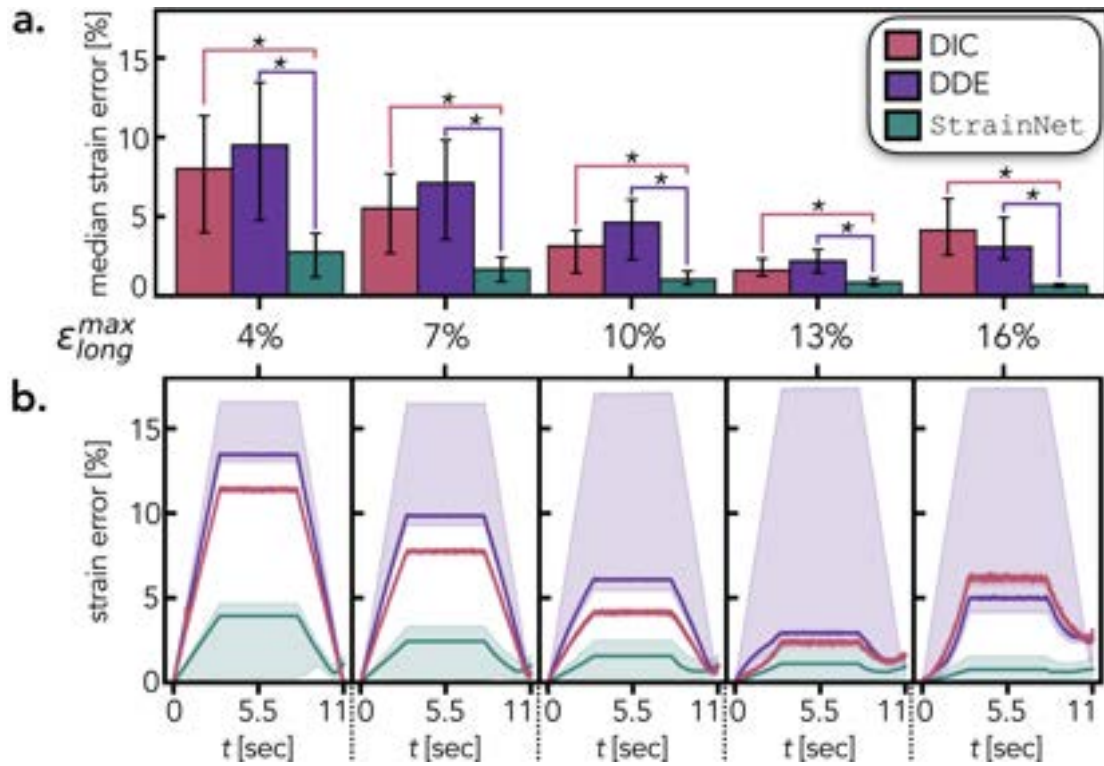
Figure 4.1: Quantitative evaluation of performance of DIC, DDE, and `StrainNet` on synthetic test cases. a. A bar plot with the median strain error calculated over all ultrasound frames and error bars indicating the first and third quartiles of the strain error. The asterisks denote a statistically significant difference with p < 0.001. **b.** Temporal strain error for each of the synthetic test cases. The solid line indicates the median strain error for each ultrasound frame and the filled-in area shows the first and third quartiles of the spatial strain error.

overall performance comparison, temporal analysis of strain error further highlights the advantages of `StrainNet` (**Figure 4.1b.**). The accuracy of `StrainNet` was as much as 88% better than DIC and DDE across all test cases (solid lines in **Figure 4.1b.**). `StrainNet` was also 90% more precise than DDE. However, DIC was the most precise of the three, outperforming `StrainNet` by nearly fourfold (filled-in area in **Figure 4.1b.**).

   `StrainNet` achieved pixel-wise strain estimation while DIC and DDE were limited to the central area of interest (**Figure 4.2a.**). DDE and `StrainNet` capture the non-linear nature of the applied
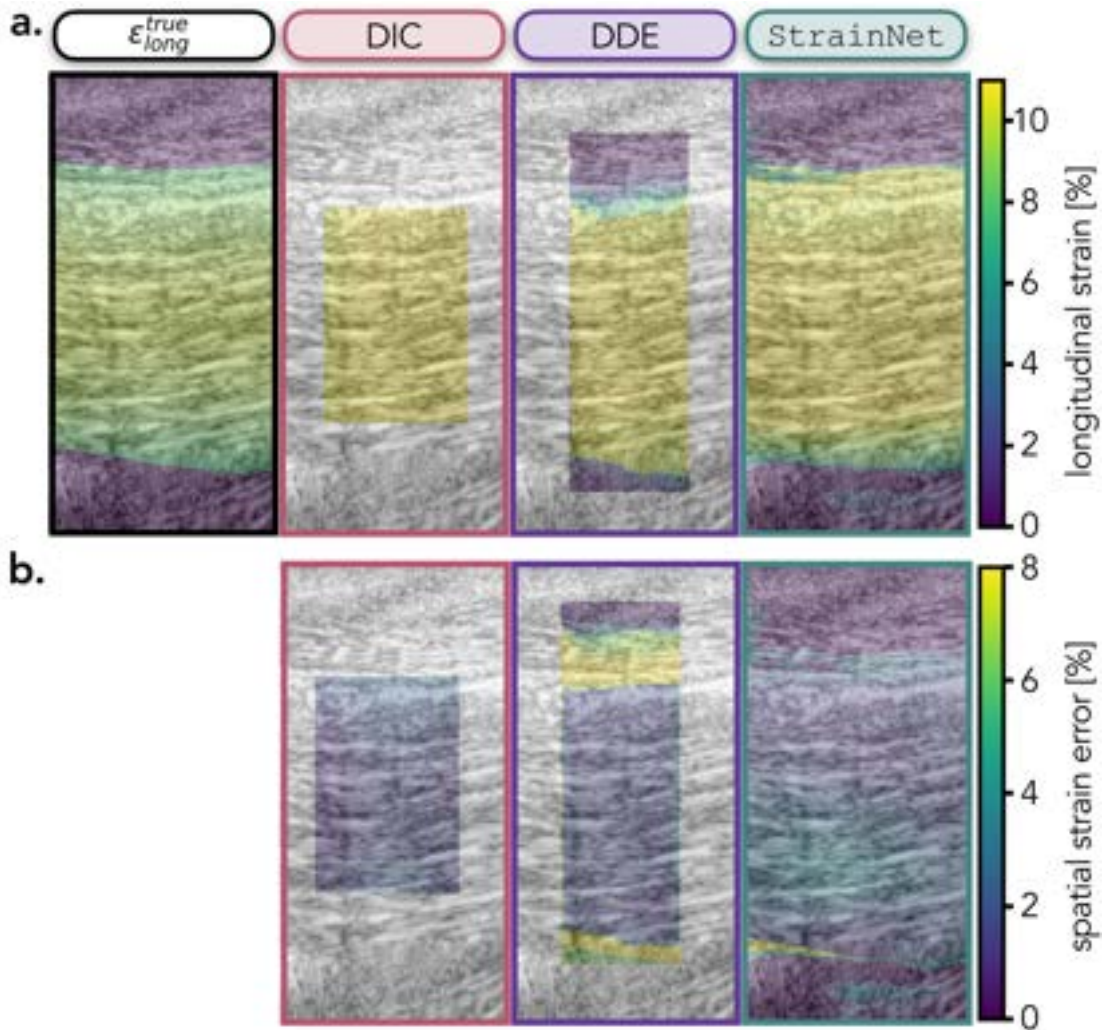
Figure 4.2: Qualitative evaluation of performance of DIC, DDE, and `StrainNet` on the synthetic test case with maximum longitudinal strain of 10% ($\varepsilon_{long}^{max} = 10\%$)**. a.** From left to right: the true prescribed and the DIC-, DDE-, and `StrainNet`-predicted longitudinal strain field during the hold period. **b.** From left to right: the DIC-, DDE-, and `StrainNet`-predicted spatial strain error distribution during the hold period.

strain, whereas the DIC-predicted strain field was homogeneous (**Figure 4.2a.**). All algorithms

exhibit low spatial strain error throughout the region of the tendon during contraction (**Figure**

4.2b.). The DIC analysis area was limited to within the boundaries of the tendon whereas DDE and

`StrainNet` cover both the tendon and the surrounding soft tissue, revealing large ($\sim$10%) spatial strain error at the boundary (**Figure 4.2b.**).

4.2   `StrainNet` ENABLES ACCURATE *IN VIVO* DEFORMATION ESTIMATION

For the *in vivo* experimental images, both DIC and DDE underperformed and many pixels were lost during image analysis. `StrainNet`, on the other hand, was able to learn around much of the noise and accurately predict the longitudinal strain in the tendon, which increased as effort level increased (**Figure 4.3a.**). There was a strong linear relationship between the `StrainNet`-predicted longitudinal strain and effort level (**Figure 4.3b.**; $r = 0.784$, $p = 0.002$). There was also a strong linear relationship between the `StrainNet`-predicted apparent modulus and effort level (**Figure 4.3c.**; $r = 0.879$, $p < 0.001$).
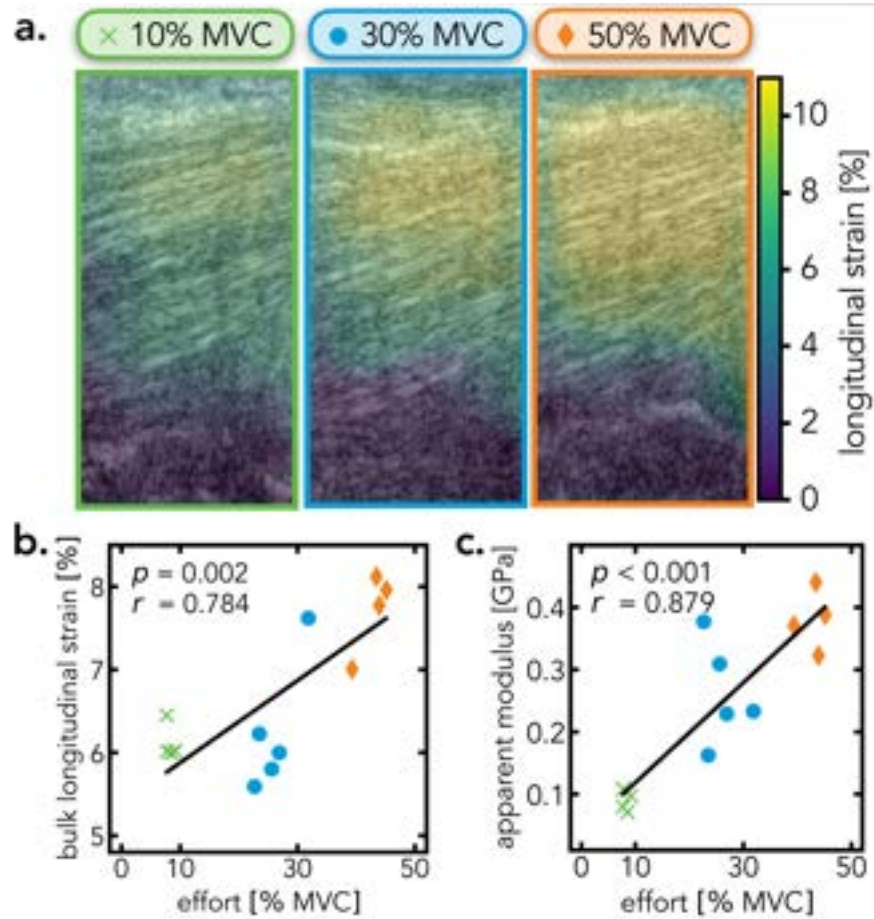
Figure 4.3: Quantitative and qualitative analysis of `StrainNet` applied to *in vivo* images. a. `StrainNet`-measured spatial distribution of longitudinal strain throughout the tendon during an isometric contraction of 10%, 30%, and 50% MVC. **b.** Linear regression between the bulk longitudinal strain along the tendon and the effort exerted by the participant (n=13 trials). **c.** Linear regression between the measured apparent modulus and the effort level (n=13 trials).

5

Discussion

StrainNet WAS ABLE TO ACCURATELY MEASURE DIFFERENT STRAIN LEVELS using ultrasound images of the flexor tendon. For synthetic datasets, StrainNet detected subtle differences in deformations with a high degree of accuracy (< 3% error), outperforming existing approaches (*e.g.*, DIC and DDE), which had median strain errors as high as 10%. Additionally, when applied to *in vivo* im-

ages, `StrainNet` predicted a strong linear correlation between the measured strain and effort level (percentage of the MVC), further validating the performance of the model. Finally, full-field deformation prediction were able to unveil stress-strain curves, and measure mechanical properties within biological tissue under physiologically relevant boundary conditions. Taken together, these findings suggest that deep learning models have the potential to significantly advance the accuracy of *in vivo* biomechanics studies.

There are several limitations to our model that will be addressed in future work. First, the model was evaluated on a single tissue type and location, so it is not clear whether it can be applied to a wider range of tissue types. Additionally, the current architecture is specialized to handle only three types of deformation, and it would be useful to explore expanding its capabilities to a wider range of deformations (*e.g.*, shear). Lastly, improvements to the architecture or training the model on a larger dataset may also allow us to remove the need for the first stage of the model, which currently classifies the type of deformation present in the image pair.

The potential applications of `StrainNet` are vast and promising. Our findings show that `StrainNet` significantly surpasses traditional image texture correlation methods in controlled environments, such as synthetic test cases (**Figure 4.1**). Moreover, in more complex settings where image texture correlation is susceptible to errors caused by image artifacts, such as real-time *in vivo* measurements of tendon mechanics, `StrainNet` consistently delivers accurate and expected tissue deformation levels (**Figure 4.3**), in line with previous reports[7,31,40]. Furthermore, the measured tissue mechanical properties align with those previously reported for human patellar and Achilles tendons *in vivo*[7,17,24,27,36] (**Table 2.1**). These results imply that `StrainNet` can be employed in a broad array

of biomedical applications, such as *in vivo* studies of muscle function, blood flow, and tissue viability. In summary, the design and capabilities of `StrainNet` hold immense potential for further research and development, leading to substantial progress in these fields.

6
Conclusion

IN THIS THESIS, `StrainNet`, a deep learning-based approach for the estimation of tissue deformation using ultrasound imaging was developed and presented. `StrainNet` demonstrated superior performance compared to traditional texture correlation techniques in both synthetic and *in vivo* images. The model was able to accurately measure and quantify strain levels in the flexor tendon,

highlighting its potential for advancing the accuracy of *in vivo* biomechanics studies.

Despite its current limitations, including the evaluation on a single tissue type and a specialized architecture for handling only three types of deformation, `StrainNet` has shown promise in its potential applications. With further development and expansion of its capabilities, `StrainNet` could be applied to a wide range of biomedical contexts, such as muscle function, blood flow, and tissue viability studies.

In conclusion, `StrainNet` presents an exciting and novel approach to tissue deformation estimation using ultrasound imaging. The results of this thesis demonstrate the model's effectiveness and provide a strong foundation for future research and development in the field of *in vivo* biomechanics and medical imaging. As the scientific community continues to explore the capabilities and applications of deep learning models, the availability of our data and code is crucial to enable further advancements in the field and facilitate the replication and extension of our findings.

Data availability

All experimental data and pre-trained models are available on reecehuff.com/StrainNet.

Code availability

The code is publically available at github.com/reecehuff/StrainNet. The project page, reecehuff.com/StrainNet, also includes a detailed tutorial for implementing `StrainNet` in any experimental setup. All data and code questions and requests should be addressed to `rdhuff@berkeley.edu`.

A

Measured error of effort level

To evaluate the discrepancy between the desired and measured effort levels during the experiments, we computed the percent root-mean-square error (RMSE) of the effort levels for 10%, 30%, and 50% MVC trials. This quantifies the deviation of the measured effort from the desired percentage of

MVC. The percent error was defined as

$$\%\text{RMSE} = \left[\frac{1}{3} \sum_{X \in [10,30,50]} \text{RMSE}(X\% \text{ MVC}) \right] \times 100$$

where

$$\text{RMSE}(X\% \text{ MVC}) = \sqrt{ \frac{1}{N_{X\% \text{ MVC}}} \sum_{i \in X\% \text{ MVC}} \left(\frac{y_i^{\text{desired}} - y_i^{\text{measured}}}{y_i^{\text{desired}}} \right)^2 }$$

where y_i^{desired} represents the desired effort level for the i-th trial at X% MVC, y_i^{measured} denotes the measured effort level for the same trial, and $N_{X\% \text{ MVC}}$ indicates the number of trials at X% MVC.

The results of this analysis are presented in Figure A.1. The red bars depict the error between the measured effort and the desired percentage of MVC for each trial. The mean RMSE over all effort levels was found to be 16%, indicating that the measured effort levels were in close agreement with the requested MVC levels.

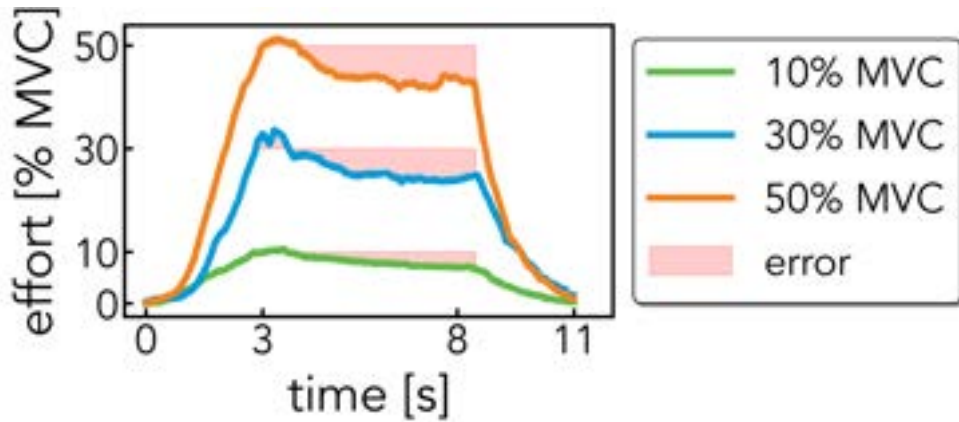**Figure A.1:** Measured effort level in a participant average over trials. The error between the measured effort and the desired percentage of the MVC is shown in red to facilitate visualization.

B

Tendon deformation model and image processing workflow

In order to train, benchmark, and tune `StrainNet`, an image-processing workflow was developed to induce known deformation within ultrasound images of tendons. This workflow was

designed for broad applicability and to emulate observed *in vivo* tendon strain.

B.1   Generalized mathematical model

Prior research has shown that deep tendon layers exhibit less strain than superficial layers[23]. Thus, a generalized strain field was specified along the tendon's length as

$$\varepsilon_{long}^{max}(y) = \frac{4(\varepsilon_{long}^{superficial} - \varepsilon_{long}^{deep})(y - y_c)^2}{h_{tendon}^{BB}} + \varepsilon_{long}^{deep} \tag{B.1}$$

where h_{tendon}^{BB} denotes the tendon's width (**Figure B.1a.**), $\varepsilon_{long}^{superficial}$ represents the longitudinal strain applied at the superficial layer, and $\varepsilon_{long}^{deep}$ signifies the longitudinal strain applied at the deep layer (**Figure B.1b.**).

While the strain distribution in Equation (B.1) characterizes tendon spatial variation, the magnitude remains uncertain. Previous studies demonstrate that tendon longitudinal strain magnitudes range between 4% and 14% during contraction[14,23,31,40] under various loading conditions. However, both the load applied and the time allowed reach the load dictate the strain magnitudes within sequential images. Consequently, the time-dependence in the prescribed strain was expressed as

$$\varepsilon_{long}^{true}(y, t) = \alpha t \varepsilon_{long}^{max}(y, t) \tag{B.2}$$

where t represents time in seconds and α is a parameter dictating the time taken for the deformation to attain its maximum. For instance, if a loading scenario reached the maximum strain in three

seconds, then α would be set to $\frac{1}{3seconds}$ to account for time dependence.

To elucidate the relationships between the longitudinal strain $\varepsilon_{long}^{true}$ defined in Equation (B.2) and the transverse strain $\varepsilon_{trans}^{true}$, the shear strain $\varepsilon_{shear}^{true}$, and the displacement field $\vec{u} = [u_x, u_y]$, a constant k is defined as

$$k = \frac{4\left(\varepsilon_{long}^{superficial} - \varepsilon_{long}^{deep}\right)}{b_{tendon}^{BB}}. \tag{B.3}$$

Hence, Equation (B.1) can be rewritten as

$$\varepsilon_{long}^{max}(y) = k(y - y_c)^2 + \varepsilon_{long}^{deep}. \tag{B.4}$$

By applying basic elasticity principles, the transverse strain field, $\varepsilon_{trans}^{true}$, can be rewritten as

$$\varepsilon_{trans}^{max}(y) = -\nu\varepsilon_{long}^{max} = -\nu\left[k(y - y_c)^2 + \varepsilon_{long}^{deep}\right] \tag{B.5}$$

The displacement field, $\vec{u} = (u_x, u_y)$, can be obtained by integrating Equation (B.4) and (B.5) with respect to x and y, respectively.

$$u_x^{max}(x, y) = kx(y - y_c)^2 + \varepsilon_{long}^{deep}x + C_1 = kx(y - y_c)^2 + \varepsilon_{long}^{deep}x \tag{B.6}$$

$$u_y^{max}(y) = -\nu\left[\frac{k(y - y_c)^3}{3} + \varepsilon_{long}^{deep}y\right] + C_2 = -\nu\left[\frac{k(y - y_c)^3}{3} + \varepsilon_{long}^{deep}(y - y_c)\right] \tag{B.7}$$

37

It should be noted that $C_1 = 0$ is set such that the displacements are small near the distal end of the tendon where x is small, and $C_2 = -\varepsilon_{long}^{deep} y_c$ is set such that $u_y = 0$ when $y = y_c$. The shear strain in the tendon then becomes

$$\varepsilon_{shear}^{max}(x, y) = \frac{1}{2}[u_{x,y} + u_{y,x}] = kx(y - y_c).$$ (B.8)

Therefore, the maximum applied strain field applied to the tendon is defined as

$$\varepsilon_{long}^{max}(y) = k(y - y_c)^2 + \varepsilon_{long}^{deep},$$ (B.9)

$$\varepsilon_{trans}^{max}(y) = -\nu\left[k(y - y_c)^2 + \varepsilon_{long}^{deep}\right],$$ (B.10)

$$\varepsilon_{shear}^{max}(x, y) = kx(y - y_c)$$ (B.11)

where $k = 4(\varepsilon_{long}^{superficial} - \varepsilon_{long}^{deep})/h_{tendon}^{BB}$. The corresponding maximum displacement field for this strain field is

$$u_x^{max}(x, y) = kx(y - y_c)^2 + \varepsilon_{long}^{deep}x$$ (B.12)

$$u_y^{max}(y) = -\nu\left[\frac{k(y - y_c)^3}{3} + \varepsilon_{long}^{deep}(y - y_c)\right]$$ (B.13)

The generalized time-dependent strain and displacement field can be expressed as

$$\varepsilon_{long}^{true}(y, t) = \alpha t \left[k(y - y_c)^2 + \varepsilon_{long}^{deep} \right] \tag{B.14}$$

$$\varepsilon_{trans}^{true}(y, t) = \alpha t \left[-\nu \left[k(y - y_c)^2 + \varepsilon_{long}^{deep} \right] \right] \tag{B.15}$$

$$\varepsilon_{shear}^{true}(x, y, t) = \alpha t \left[kx(y - y_c) \right] \tag{B.16}$$

$$u_x^{true}(x, y, t) = \alpha t \left[kx(y - y_c)^2 + \varepsilon_{long}^{deep} x \right] \tag{B.17}$$

$$u_y^{true}(y, t) = \alpha t \left[-\nu \left[\frac{k(y - y_c)^3}{3} + \varepsilon_{long}^{deep}(y - y_c) \right] \right] \tag{B.18}$$

The strain field and displacement field were only defined over the region of the image containing the tendon (**Figure B.1b.**). Regions containing tendon were defined semi-automatically with ImageJ [38] (U.S. National Institutes of Health, Bethesda, Maryland, USA).

B.2 Prescribed image deformation and noise addition

Images were artificially deformed by the prescribed displacement field (Equation (B.17) and (B.18)) over the region of the tendon using MATLAB's `imwarp` function with linear interpolation settings (MATLAB version R2021b; **Figure B.1c.**).

The level of noise added to the image was defined by analyzing a series of frames with a stationary participant's arm. The differences between the image intensities of the frames were analyzed, and the mean and standard deviation of the intensity differences were calculated. Across all frames analyzed ($n = 2000$), it was found that the noise levels remain approximately normally distributed with

a mean of 0 and a standard deviation of 10. Therefore, MATLAB's randn function was used to add

a random distribution of noisy pixel intensities to the frames of the synthetic test case. To match the

noise levels measured experimentally, $\mu = 0$ and $\sigma = 10$ were set in randn (**Figure B.1c.**).
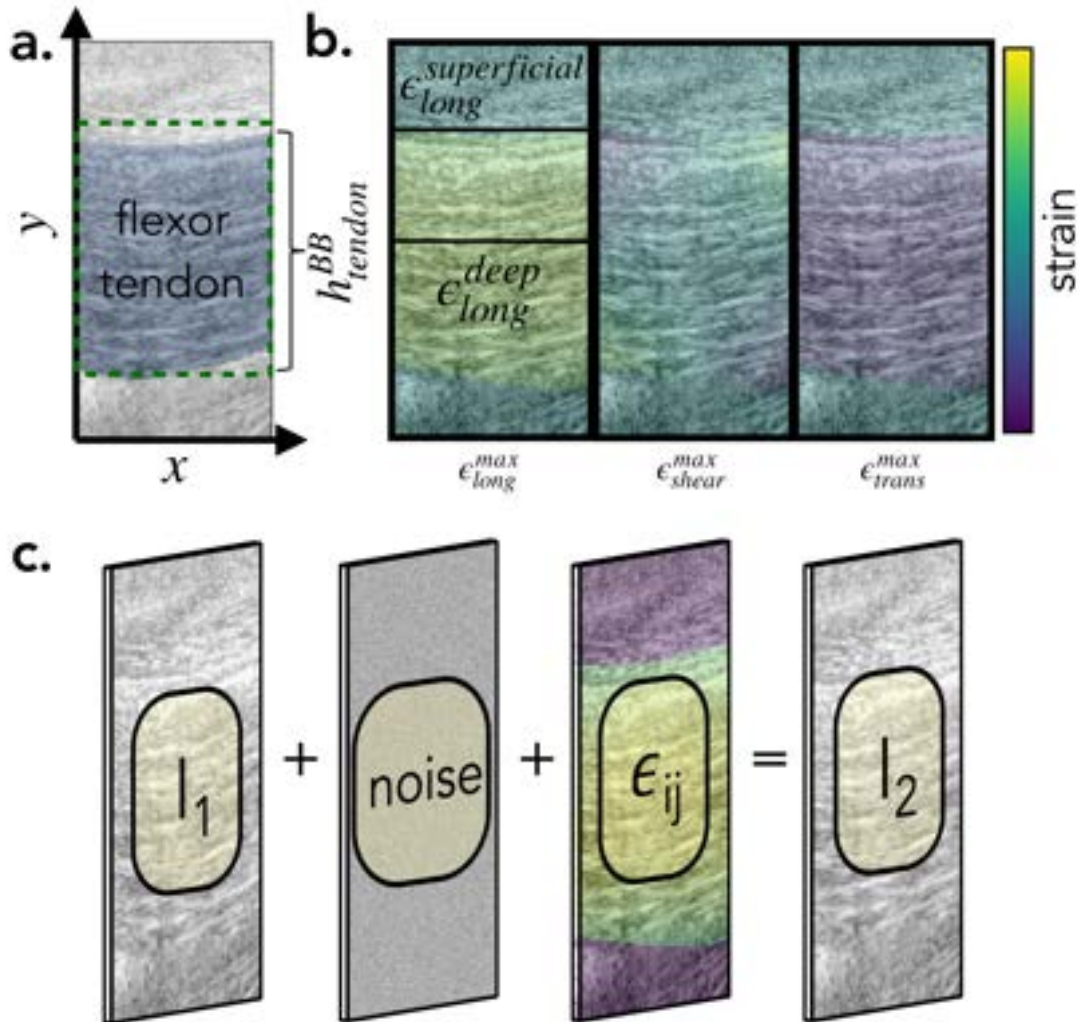
Figure B.1: Diagram of tendon deformation model and ultrasound image processing workflow. a. A representative ultrasound image containing a flexor tendon, shaded in blue, with a height, h_{tendon}^{BB}, green dashed box used in Equation B.1. **b.** A strain distribution resulting from the generalized mathematical model, ε_{long}^{max}, $\varepsilon_{shear}^{max}$, and $\varepsilon_{trans}^{max}$, values defined by Equation B.9, Equation B.11, and Equation B.10 respectively, illustrating the regions where these equations were applied. **c.** The general workflow of the image processing pipeline. A reference tendon image, I_1, was warped by the generalized mathematical model, noise was introduced, resulting in a deformed image, I_2.

C

Training set generation

C.1 Overview

To train `StrainNet`, we created a training set containing ultrasound images of tendon deformation with corresponding strain fields. The training set was composed of both synthetically generated images and experimental data, which were processed and combined to ensure a diverse and representative dataset for learning the strain measurement task. Here, we describe the process of generating

the training set, including the acquisition of experimental data, image preprocessing, and the combination of synthetic and experimental cases.

C.2   Experimental data acquisition

We conducted an addition, independent ultrasound imaging session using the same protocol described in **Section 3.2**. In short, the participant performed a series of contractions, holding each contraction for 5 seconds, followed by a 3-second relaxation period. This protocol allowed us to capture a range of tendon strains during both contraction and relaxation phases. The captured ultrasound images were then used to generate a dataset for the training set creation.

C.3   Image preprocessing

Before incorporating the experimental data into the training set, we performed several preprocessing steps to ensure the images were suitable for training. The preprocessing steps included:

- **Region of Interest (ROI) selection:** The *flexor digitorum superficialis* (FDS) tendon was manually identified and segmented in each ultrasound image. This step focused the training on the relevant tendon deformation while ignoring motion and strain in the surrounding soft tissue.

- **Image normalization:** The pixel intensities of each image were normalized to have a mean of zero and a standard deviation of one. This normalization step facilitated the training process by ensuring consistent image intensity values across the dataset.

- **Augmentation:** To increase the diversity and size of the dataset, we applied various augmentation techniques, including rotations and translations. These augmentations helped the neural network learn to recognize tendon deformation patterns in various contexts and improved the generalization capability of the trained model.

C.4 Application of the generalized mathematical model

The workflow described in **Appendix B** was combined with the preprocessed experimental data to create a comprehensive training set for `StrainNet`. Specifically, the mathematical model described in Equations (B.14) - (B.18) was employed, where the mechanics properties were selected at random. Noise was added to each of the images to emulate real image artifacts, as detailed in **Section B.2**. The synthetic cases provided known strain fields, enabling the neural network to learn the relationships between the ultrasound images and the corresponding strain fields. Meanwhile, the experimental data ensured that the neural networks were exposed to real-world tendon deformation patterns.

Table C.1: Randomly selected mechanical properties for training set generation.

model	n	ε_{long}^{sup} & $\varepsilon_{long}^{deep}$	αt	ν	h_{tendon}^{BB} & y_c	exp. aug.[γ]	noise ($\mu \pm \sigma$)
TensionNet	1,250	[2,20]			measured	N	
RigidNet	1,250	[-20,20][α]	$\left[\frac{1}{15}, \frac{1}{5}\right]$	[0.25,1.5]	from	N	0 ± 10
CompressionNet	1,250	[-20,-2]			image[β]	N	
Deformation Classifier	3,750 +1,250[γ]	—pool examples from above—				Y	

[α]While the images were warped by these largest parameters, the warped image was used for the reference and deformed image.
[β]**Figure D.1a.** highlights the measurement of h_{tendon}^{BB} & y_c.
[γ] Experimental augmentation whereby experimental images with tensile deformation (during contraction), compressive deformation (during relaxation), and rigid-body motions (during static periods) are included in the training of the `DeformationClassifier`.

In total, the training set consisted of 5,000 ultrasound image pairs with known strain fields and added noise—1,250 examples of tensile deformation, compressive deformation, and rigid-body motions for `TensionNet`, `CompressionNet`, and `RigidNet`, respectively (**Table C.1**). All 3,750 ex-

amples were used to train the `DeformationClassifier`. Additionally, 1,250 experimental images were included, where the tendon was assumed to undergo tensile deformation, rigid-body motions, and compressive deformation during the contraction, the hold period, and the relaxation, respectively (**Table C.1**). The strain fields corresponding to each image were included into the training set, serving as the ground truth during the training process.

D

Synthetic test cases

To benchmark and tune the strain measurement techniques, a series of idealized test cases were created where the applied strain was known. To mimic the experimental procedure detailed in **Section 3.2**, the mathematical model outlined in **Appendix B** was modified to reach its peak after a contraction period of three seconds. This peak was then maintained for five seconds,
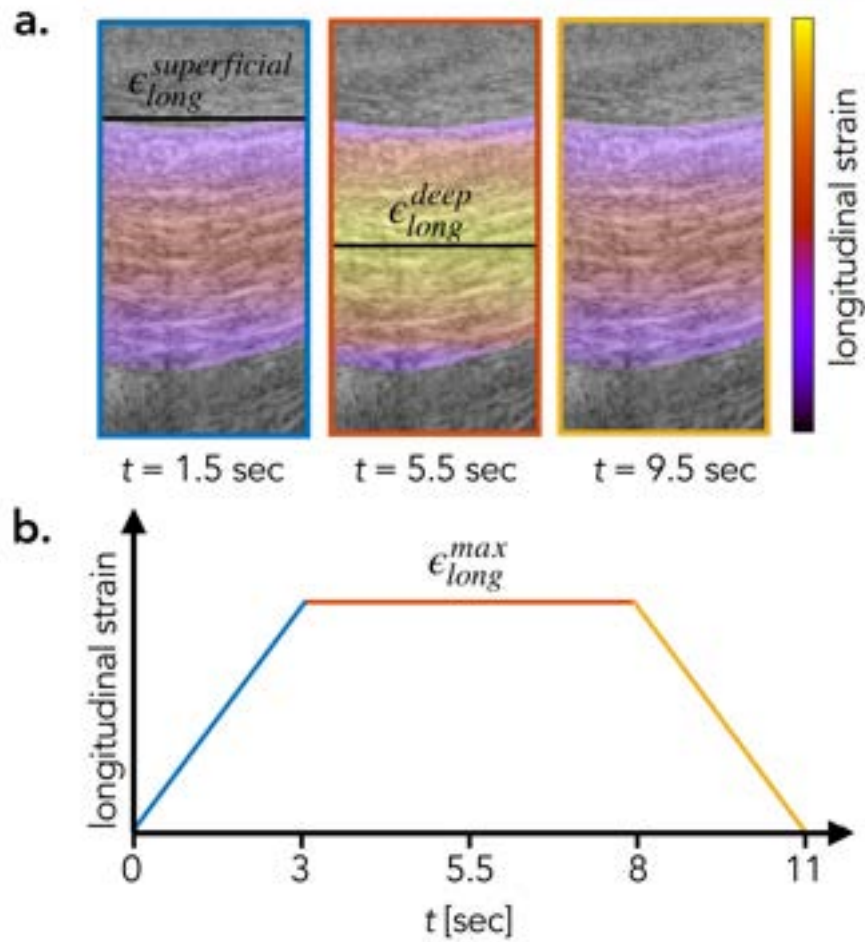
Figure D.1: An overview of synthetic test cases for assessing tendon deformation using ultrasound imaging. a. Longitudinal strain distribution, $\varepsilon_{long}^{true}$, at t = 1.5, 5.5, and 9.5 seconds. **b.** The time-dependent change in the maximum prescribed longitudinal strain, ε_{long}^{max}, over the course of the synthetic test cases. Blue, red, and yellow represent periods of contraction, holding, and relaxation, respectively.

followed by a relaxation period of three seconds (**Figure D.1**). As a result, the true time-dependent

strain field was defined as

$$
\varepsilon_{long}^{true}(y, t) =
\begin{cases}
\left(\frac{t}{3}\right)\varepsilon_{long}^{max}(y) & \text{for } 0 \text{ sec} \leq t \leq 3 \text{ sec} \\[2em]
\varepsilon_{long}^{max}(y) & \text{for } 3 \text{ sec} < t \leq 8 \text{ sec} \\[2em]
\left(1 - \frac{t-8}{3}\right)\varepsilon_{long}^{max}(y) & \text{for } 8 \text{ sec} < t \leq 11 \text{ sec}
\end{cases}
\tag{D.1}
$$

$$
\varepsilon_{trans}^{true}(y, t) =
\begin{cases}
\left(\frac{t}{3}\right)\varepsilon_{trans}^{max}(y) & \text{for } 0 \text{ sec} \leq t \leq 3 \text{ sec} \\[2em]
\varepsilon_{trans}^{max}(y) & \text{for } 3 \text{ sec} < t \leq 8 \text{ sec} \\[2em]
\left(1 - \frac{t-8}{3}\right)\varepsilon_{trans}^{max}(y) & \text{for } 8 \text{ sec} < t \leq 11 \text{ sec}
\end{cases}
\tag{D.2}
$$

$$
\varepsilon_{shear}^{true}(x, y, t) =
\begin{cases}
\left(\frac{t}{3}\right)\varepsilon_{shear}^{max}(y) & \text{for } 0 \text{ sec} \leq t \leq 3 \text{ sec} \\[2em]
\varepsilon_{shear}^{max}(x, y) & \text{for } 3 \text{ sec} < t \leq 8 \text{ sec} \\[2em]
\left(1 - \frac{t-8}{3}\right)\varepsilon_{shear}^{max}(x, y) & \text{for } 8 \text{ sec} < t \leq 11 \text{ sec}
\end{cases}
\tag{D.3}
$$

and the full time-dependent prescribed displacement field was

$$
u_x^{true}(x, y, t) = \begin{cases} \left(\frac{t}{3}\right)u_x^{max}(x, y) & \text{for } 0 \text{ sec} \leq t \leq 3 \text{ sec} \\\\ u_x^{max}(x, y) & \text{for } 3 \text{ sec} < t \leq 8 \text{ sec} \\\\ \left(1 - \frac{t-8}{3}\right)u_x^{max}(x, y) & \text{for } 8 \text{ sec} < t \leq 11 \text{ sec} \end{cases} \tag{D.4}
$$

$$
u_y^{true}(y, t) = \begin{cases} \left(\frac{t}{3}\right)u_y^{max}(y) & \text{for } 0 \text{ sec} \leq t \leq 3 \text{ sec} \\\\ u_y^{max}(y) & \text{for } 3 \text{ sec} < t \leq 8 \text{ sec} \\\\ \left(1 - \frac{t-8}{3}\right)u_y^{max}(y) & \text{for } 8 \text{ sec} < t \leq 11 \text{ sec} \end{cases} \tag{D.5}
$$

Additionally, studies have shown that tendons exhibit longitudinal strain magnitudes between 4% and 14% under contraction, and therefore the maximum applied strain, which occurs where $y = y_c$, was varied between 4% and 16% [14,23,31,40] over five different synthetic test cases (**Table D.1**). We assumed that the tendon was incompressible; therefore, the Poisson's ratio was 0.5 throughout the tendon (**Table D.1**)[47].

Table D.1: Summary of the five synthetic test cases used to evaluate, tune, and validate the three strain measurement techniques: DIC, DDE, StrainNet.

Test Case	ε_{long}^{max}	$\varepsilon_{long}^{superficial}$	ν	Contraction time	Hold time	Relaxation time
1	4%	3%	0.5	3 sec	5 sec	3 sec
2	7%	5.25%	0.5	3 sec	5 sec	3 sec
3	10%	7.5%	0.5	3 sec	5 sec	3 sec
4	13%	9.75%	0.5	3 sec	5 sec	3 sec
5	16%	12%	0.5	3 sec	5 sec	3 sec

Bibliography

[1] Blachut, K. & Kryjak, T. (2022). Real-time efficient fpga implementation of the multi-scale lucas-kanade and horn-schunck optical flow algorithms for a 4k video stream. *Sensors*, 22(13), 5017.

[2] Bornert, M., Brémand, F., Doumalin, P., Dupré, J.-C., Fazzini, M., Grédiac, M., Hild, F., Mistou, S., Molimard, J., Orteu, J.-J., et al. (2009). Assessment of digital image correlation measurement errors: methodology and results. *Experimental mechanics*, 49, 353–370.

[3] Bornert, M., Doumalin, P., Dupré, J.-C., Poilâne, C., Robert, L., Toussaint, E., & Wattrisse, B. (2012). Short remarks about synthetic image generation in the context of sub-pixel accuracy of digital image correlation. In *ICEM15-15th International Conference on Experimental Mechanics* (pp. 9–p).

[4] Boukhtache, S., Abdelouahab, K., Berry, F., Blaysat, B., Grediac, M., & Sur, F. (2021). When deep learning meets digital image correlation. *Optics and Lasers in Engineering*, 136, 106308.

[5] Boyle, J. J., Kume, M., Wyczalkowski, M. A., Taber, L. A., Pless, R. B., Xia, Y., Genin, G. M., & Thomopoulos, S. (2014). Simple and accurate methods for quantifying deformation, disruption, and development in biological tissues. *Journal of The Royal Society Interface*, 11(100), 20140685.

[6] Boyle, J. J., Soepriatna, A., Damen, F., Rowe, R. A., Pless, R. B., Kovacs, A., Goergen, C. J., Thomopoulos, S., & Genin, G. M. (2018). Regularization-Free Strain Mapping in Three Dimensions, With Application to Cardiac Ultrasound. *Journal of Biomechanical Engineering*, 141(1).

[7] Carroll, C. C., Dickinson, J. M., Haus, J. M., Lee, G. A., Hollon, C. J., Aagaard, P., Magnusson, S. P., & Trappe, T. A. (2008). Influence of aging on the in vivo properties of human patellar tendon. *Journal of applied physiology*, 105(6), 1907–1915.

[8] Coombes, B. K., Tucker, K., Hug, F., & Dick, T. J. (2020). Age-related differences in gastrocnemii muscles and achilles tendon mechanical properties in vivo. *Journal of biomechanics*, 112, 110067.

[9] Dosovitskiy, A., Fischer, P., Ilg, E., Hausser, P., Hazirbas, C., Golkov, V., Van Der Smagt, P., Cremers, D., & Brox, T. (2015). Flownet: Learning optical flow with convolutional networks. In *Proceedings of the IEEE international conference on computer vision* (pp. 2758–2766).

[10] Drozdzal, M., Vorontsov, E., Chartrand, G., Kadoury, S., & Pal, C. (2016). The importance of skip connections in biomedical image segmentation. In *International Workshop on Deep Learning in Medical Image Analysis, International Workshop on Large-Scale Annotation of Biomedical Data and Expert Label Synthesis* (pp. 179–187).: Springer.

[11] Dutton, M., Take, W. A., & Hoult, N. A. (2014). Curvature monitoring of beams using digital image correlation. *Journal of Bridge Engineering*, 19(3), 05013001.

[12] Earl, C. C., Damen, F. W., Yin, M., Aasa, K. L., Burris, S. K., & Goergen, C. J. (2021). Strain estimation of the murine right ventricle using high-frequency speckle-tracking ultrasound. *Ultrasound in Medicine and Biology*, 47(11), 3291–3300.

[13] Gao, Z., Xu, X., Su, Y., & Zhang, Q. (2016). Experimental analysis of image noise and interpolation bias in digital image correlation. *Optics and Lasers in Engineering*, 81, 46–53.

[14] Gerus, P., Rao, G., & Berton, E. (2011). A method to characterize in vivo tendon force–strain relationship by combining ultrasonography, motion capture and loading rates. *Journal of Biomechanics*, 44(12), 2333–2336.

[15] Goenezen, S., Dord, J.-F., Sink, Z., Barbone, P. E., Jiang, J., Hall, T. J., & Oberai, A. A. (2012). Linear and nonlinear elastic modulus imaging: An application to breast cancer diagnosis. *IEEE Transactions on Medical Imaging*, 31(8), 1628–1637.

[16] Han, Y., Kim, D.-W., & Kwon, H.-J. (2012). Application of digital image cross-correlation and smoothing function to the diagnosis of breast cancer. *Journal of the Mechanical Behavior of Biomedical Materials*, 14, 7–18.

[17] Hansen, P., Bojsen-Moller, J., Aagaard, P., Kjaer, M., & Magnusson, S. P. (2006). Mechanical properties of the human patellar tendon, in vivo. *Clinical Biomechanics*, 21(1), 54–58.

[18] Hokka, M., Mirow, N., Nagel, H., Irqsusi, M., Vogt, S., & Kuokkala, V.-T. (2015). In-vivo deformation measurements of the human heart by 3d digital image correlation. *Journal of Biomechanics*, 48(10), 2217–2220.

[19] Holsgrove, T. P., Cazzola, D., Preatoni, E., Trewartha, G., Miles, A. W., Gill, H. S., & Gheduzzi, S. (2015). An investigation into axial impacts of the cervical spine using digital image correlation. *The Spine Journal*, 15(8), 1856–1863.

[20] Horn, B. K. & Schunck, B. G. (1981). Determining optical flow. *Artificial intelligence*, 17(1-3), 185–203.

[21] Hussein, A. I., Barbone, P. E., & Morgan, E. F. (2012). Digital volume correlation for study of the mechanics of whole bones. *Procedia IUTAM*, 4, 116–125. IUTAM Symposium on Full-field Measurements and Identification in Solid Mechanics.

[22] Kubo, K., Kanehisa, H., Ito, M., & Fukunaga, T. (2001). Effects of isometric training on the elasticity of human tendon structures in vivo. *Journal of applied physiology*, 91(1), 26–32.

[23] Lee, D., Barrett, R., Ryan, M., Saxby, D. J., Newsham-West, R., & Obst, S. J. (2017). In vivo strain in the deep and superficial regions of the human patellar tendon. *Scandinavian Journal of Medicine & Science in Sports*, 27(10), 1105–1113.

[24] Lichtwark, G. A. & Wilson, A. (2005). In vivo mechanical properties of the human achilles tendon during one-legged hopping. *Journal of experimental biology*, 208(24), 4715–4725.

[25] Loaiza, J. (2021). *Digital volume correlation as a method for estimating load-induced deformations in the human spine*. PhD thesis, Boston University.

[26] Lucas, B. D., Kanade, T., et al. (1981). An iterative image registration technique with an application to stereo vision. In *Intl Joint Conf on Artificial Intelligence*.

[27] Maganaris, C. N. & Paul, J. P. (1999). In vivo human tendon mechanical properties.

[28] Mathieu, F., Hild, F., & Roux, S. (2012). Identification of a crack propagation law by digital image correlation. *International Journal of Fatigue*, 36(1), 146–154.

[29] Mazzoleni, P., Matta, F., Zappa, E., Sutton, M. A., & Cigada, A. (2015). Gaussian pre-filtering for uncertainty minimization in digital image correlation using numerically-designed speckle patterns. *Optics and Lasers in Engineering*, 66, 19–33.

[30] Montesano, J., Selezneva, M., Levesque, M., & Fawaz, Z. (2015). Modeling fatigue damage evolution in polymer matrix composite structures and validation using in-situ digital image correlation. *Composite Structures*, 125, 354–361.

[31] O'Brien, T. D., Reeves, N. D., Baltzopoulos, V., Jones, D. A., & Maganaris, C. N. (2010). Mechanical properties of the patellar tendon in adults and children. *Journal of Biomechanics*, 43(6), 1190–1195.

[32] Palanca, M., Tozzi, G., & Cristofolini, L. (2016). The use of digital image correlation in the biomechanical area: a review. *International Biomechanics*, 3(1), 1–21.

[33] Pan, B., Li, K., & Tong, W. (2013). Fast, robust and accurate digital image correlation calculation without redundant computations. *Experimental Mechanics*, 53, 1277–1289.

[34] Paszke, A., Gross, S., Massa, F., Lerer, A., Bradbury, J., Chanan, G., Killeen, T., Lin, Z., Gimelshein, N., Antiga, L., et al. (2019). Pytorch: An imperative style, high-performance deep learning library. *Advances in neural information processing systems*, 32.

[35] Peters, W. H. & Ranson, W. F. (1982). Digital Imaging Techniques In Experimental Stress Analysis. *Optical Engineering*, 21(3), 427–431.

[36] Reeves, N. D., Maganaris, C. N., & Narici, M. V. (2003). Effect of strength training on human patella tendon mechanical properties of older individuals. *The Journal of physiology*, 548(3), 971–981.

[37] Ronneberger, O., Fischer, P., & Brox, T. (2015). U-net: Convolutional networks for biomedical image segmentation. In N. Navab, J. Hornegger, W. M. Wells, & A. F. Frangi (Eds.), *Medical Image Computing and Computer-Assisted Intervention – MICCAI 2015* (pp. 234–241). Cham: Springer International Publishing.

[38] Schneider, C. A., Rasband, W. S., & Eliceiri, K. W. (2012). Nih image to imagej: 25 years of image analysis. *Nature methods*, 9(7), 671–675.

[39] Schreier, H., Orteu, J.-J., Sutton, M. A., Michael A, M. A., Orteu, J.-J., & Schreier, H. W. (2009). Digital image correlation (dic). *Image Correlation for Shape, Motion and Deformation Measurements: Basic Concepts, Theory and Applications*, (pp. 1–37).

[40] Sheehan, F. T. & Drace, J. E. (2000). Human patellar tendon strain: a noninvasive, in vivo study. *Clinical Orthopaedics and Related Research*, 370, 201–207.

[41] Shi, X., Huang, Z., Li, D., Zhang, M., Cheung, K. C., See, S., Qin, H., Dai, J., & Li, H. (2023). Flowformer++: Masked cost volume autoencoding for pretraining optical flow estimation. *arXiv preprint arXiv:2303.01237*.

[42] Siebert, T., Becker, T., Spiltthof, K., Neumann, I., & Krupka, R. (2007). High-speed digital image correlation: error estimations and applications. *Optical Engineering*, 46(5), 051004–051004.

[43] Sutton, M. A. & Hild, F. (2015). Recent advances and perspectives in digital image correlation. *Experimental Mechanics*, 55(1), 1–8.

[44] Suydam, S. M. & Buchanan, T. S. (2014). Is echogenicity a viable metric for evaluating tendon properties in vivo? *Journal of biomechanics*, 47(8), 1806–1809.

[45] Teed, Z. & Deng, J. (2020). Raft: Recurrent all-pairs field transforms for optical flow. In *Computer Vision–ECCV 2020: 16th European Conference, Glasgow, UK, August 23–28, 2020, Proceedings, Part II 16* (pp. 402–419).: Springer.

[46] Triconnet, K., Derrien, K., Hild, F., & Baptiste, D. (2009). Parameter choice for optimized digital image correlation. *Optics and lasers in Engineering*, 47(6), 728–737.

[47] Vergari, C., Pourcelot, P., Holden, L., Ravary-Plumioën, B., Gerard, G., Laugier, P., Mitton, D., & Crevier-Denoix, N. (2011). True stress and poisson's ratio of tendons during loading. *Journal of Biomechanics*, 44(4), 719–724.

[48] Wang, G., Zhang, L., & Yao, X. (2022). Strainnet-3d: Real-time and robust 3-dimensional speckle image correlation using deep learning. *Optics and Lasers in Engineering*, 158, 107184.

[49] Wang, Y., Sutton, M., Bruck, H., & Schreier, H. (2009). Quantitative error assessment in pattern matching: effects of intensity pattern noise, interpolation, strain and image contrast on motion measurements. *Strain*, 45(2), 160–178.

[50] Wang, Z., Li, H., Tong, J., & Ruan, J. (2007). Statistical analysis of the effect of intensity pattern noise on the displacement measurement precision of digital image correlation using self-correlated images. *Experimental Mechanics*, 47(5), 701–707.

[51] Yang, R., Li, Y., Zeng, D., & Guo, P. (2022). Deep dic: Deep learning-based digital image correlation for end-to-end displacement and strain measurement. *Journal of Materials Processing Technology*, 302, 117474.

Reece D. **Huff**

COMPUTATIONAL BIOMECHANICS · MACHINE LEARNING · OPTIMIZATION

☐ (+1) 651-402-0037 | ✉ rdhuff@berkeley.edu | ⌂ reecehuff.com | ⌨ reecehuff | in reece-huff

Summary

I am a Mechanical Engineering Ph.D. student in the Berkeley BioMechanics Laboratory. I am passionate about harnessing the power of deep learning to synergize medical imaging techniques, such as ultrasound, with motion capture systems in order to unravel the underlying mechanisms contributing to musculoskeletal disorders. My expertise in handling large, noisy datasets, as well as my strong programming skills, allow me to effectively develop innovative solutions for complex biomedical challenges.

Education

University of California, Berkeley   *Berkeley, CA*
PH.D. IN MECHANICAL ENGINEERING   *Aug. 2021 - May 2026*
- Advisors: Grace O'Connell & Jeannie Bailey
- Awards: NSF GRFP, Graduate Division Block Grant

University of California, Berkeley   *Berkeley, CA*
M.S. IN MECHANICAL ENGINEERING (GPA: 3.96/4.00)   *Aug. 2021 - May 2023*
- Major: Biomechanical Engineering, Minors: Computer Science & Statistics

Boston University   *Boston, MA*
B.S. IN BIOMEDICAL ENGINEERING (GPA: 3.99/4.00)   *Aug. 2018 - May 2021*
- Advisors: Elise Morgan & Paul Barbone
- Awards: Goldwater Scholarship, Distinguished Summer Research Fellowship

Skills

Programming	Python • C/C++ • Julia • HTML+CSS • SQL • Bash • LaTeX • Git • MATLAB • Mathematica
Software	TensorFlow • Tensorboard • PyTorch • CUDA • CVXPY • pandas • sklearn • OpenMP • MPI • OpenCL
Techniques	Deep learning • data science • computer vision • markerless motion capture • finite element modeling
General	Google Suite • Adobe Creative Cloud • Microsoft Office

Publications

2023	**Deep learning enables accurate *in vivo* deformation prediction**, in preparation	project page
2022	**Comparing intervertebral disc geometry measurement method**, JOR Spine	paper • project page
2022	**Finite-element modeling of lumbar disc herniation**, JBME	paper • project page

Experience

University of California, Berkeley   *Berkeley, CA*
GRADUATE RESEARCH ASSISTANT   *Aug. 2021 - present*
- Developed a novel deep-learning approach for measuring *in vivo* tissue deformation
- Modeled muscle- and torque-driven flexion to the intervertebral disc

Boston University   *Boston, MA*
UNDERGRADUATE RESEARCH ASSISTANT   *Mar. 2019 - Aug. 2021*
- Optimized bone tracking algorithm that measures the displacement field in a fracturing vertebra
- Created a novel framework for providing voxel-by-voxel accuracy evaluations of 3D optical flow algorithms

Coursework

Mechanics	Orthopedic Biomechanics, Biomaterials, Finite Element Modeling, Continuum Mechanics, Elasticity, Fluid Mechanics, Thermodynamics, Statics, Dynamics, Statistical Mechanics
Computational	Machine Learning, Parallel Computing, Reinforcement Learning, Computational Linear Algebra, Numerical Methods
Mathematics	Applied Mathematics, Linear Algebra, Probability, Statistics, Advanced Calculus, Differential Equations
General	Physics, Chemistry, Molecular Biology, Engineering Design, Circuits, Physiology